INTERNATIONAL JOURNAL FOR NUMERICAL METHODS IN FLUIDS, VOL. 24, 537–561 (1997)

MODELLING OF FLOW IN RECTANGULAR SEDIMENTATION TANKS BY AN EXPLICIT THIRD-ORDER UPWINDING TECHNIQUE

HANY GERGES AND JOHN A. McCORQUODALE

Department of Civil and Environmental Engineering, University of Windsor, Windsor, Ont. N9B 3P4, Canada

SUMMARY

A new numerical model has been developed to simulate the transport of dye in primary sedimentation tanks operating under neutral density conditions. A multidimensional algorithm based on a new skew third-order upwinding scheme (STOUS) is used to eliminate numerical diffusion. This algorithm introduces cross-difference terms to overcome the instability problems of the componentwise one-dimensional formlae for simulating multidimensional flows. Small physically unrealistic overshooting and undershooting have been avoided by using a well-established technique known as the universal limiter. A well-known rotating velocity field test was used to show the capability of STOUS in eliminating numerical diffusion. The STOUS results are compared with another third-order upwinding technique known as UTOPIA. The velocity field is obtained by solving the equations of motion in the vorticity–streamfunction formulation. A k–ϵ model is used to simulate the turbulence phenomena. The velocity field compares favourably with previous measurements and with UTOPIA results. An additional differential equation governing the unsteady transport of dye in a steady flow field is solved to calculate the dye concentration and to produce flow-through curves (FTCs) which are used in evaluating the hydraulic efficiency of settling tanks. The resulting FTC was compared with both measurements and numerical results predicted by various discretization schemes.

KEY WORDS: third-order upwinding; numerical diffusion; numerical instabilities; dye transport; sedimentation tank

1. INTRODUCTION

The lack of an accurate simulation of one-dimensional highly convective unsteady flows has been referred to as the 'ultimate embarrassment'.[1] Second-order central schemes can simulate smooth profiles (low curvature) with satisfactory accuracy; however, these schemes suffer from numerical oscillations when a sudden change in gradient (high curvature) exists. This is due to the inherent spatial dispersion terms (third derivative) in the truncation error. First-order upwinding can handle sharp profiles, but the spatial second-derivative terms in the truncation error overwhelm any physical diffusion.[2] Second-order upwinding is considered to be better than second-order central and first-order upwinding schemes. The leading-order truncation error is a dispersive third derivative; however, in some cases the dissipation derivative terms are stronger and dampen dispersive oscillations.[3] Fromm[4] introduced a convection algorithm in which he averaged second-order upwinding with the explicit second-order central scheme.[5] In this algorithm the leading phase error of the upwind difference approximately cancels the lagging phase error of the central scheme.

CCC 0271–2091/97/060537–25 $17.50

Received 5 December 1994
Revised 29 May 1996

Leonard[6] introduced two convection algorithms based on spatial quadratic upstream interpolation schemes. The first one is for steady state and is referred to as QUICK (quadratic upstream interpolation for convective kinematics), while the other is for unsteady simulation and is known as QUICKEST (QUICK with estimated streaming terms). QUICKEST is an explicit third-order upwinding scheme and has a high-order spatial approximation accompanied by a consistently accurate temporal formulation. The leading truncation error is of a dissipative type (fourth order) and of a higher order than the physical diffusion[3] with the diffusion terms modelled to a consistent order. The use of higher-order spatial approximations with a lower-order temporal formulation would be equivalent to first-order upwinding in resolving the unsteady features.[7] Schemes based on the use of time–space characteristics have been formulated and applied by several researchers.[8–10]

The third-order upwinding approach was first introduced by Leonard,[6] who later showed this to be the rational basis for computational fluid dynamics;[11] however, a large number of researchers are still using first-order upwinding (or the hybrid scheme) as a robust way of modelling highly convective flows. First-order upwinding or any other technique which suffers from numerical diffusion adds artificial viscosity to the physical viscosity. Leonard and Niknafs[3] as well as Leschziner and Rodi[12] indicated that it does not make sense to use a highly sophisticated multiequation turbulence model to determine the eddy viscosity while the equations of motion are modelled with a convective scheme suffering from numerical diffusion.

Third-order upwinding schemes are susceptible to physically unrealistic overshooting and undershooting of the order of 5%. Although these oscillations are small compared with the other methods, they may cause problems when solving the non-linear equations of motion. These oscillations can be eliminated by using a well-established technique known as the universal limiter.[13]

The extension of a one-dimensional (1D) unsteady algorithm to two dimensions is another serious problem, since 1D algorithms do not automatically generalize to two and three dimensions by applying the one-dimensional scheme componentwise.[14] This is due to the absence of the cross-terms in the Taylor expansion. Leonard and Niknafs[15] developed a high-accuracy algorithm using the concept of vector transient interpolation modelling:

$$\Phi(x, t + \Delta t) = \Phi(x - v\Delta t, t). \tag{1}$$

Using this concept, they introduced multidimensional first-order upwinding, second-order central and third-order upwinding algorithms for square grids. The third-order upwinding algorithm was referred to as UTOPIA (uniformly third-order polynomial interpolation algorithm). This can be considered to be an extension of the one-dimensional QUICKEST scheme.[6] They evaluated the performance of the different algorithms by using a well-known rotating velocity field convection problem as a benchmark test. Two non-oscillatory total-variation-diminishing (TVD) schemes designed by Roe[16] were also tested. The TVD-Minmod scheme was found to be quite diffusive, while the TVD-Superbee scheme tended to steepen and clip narrow extrema. They also made a Fourier–von Neumann analysis[17,18] of the multidimensional algorithms and compared Taylor expansions of their complex amplitude ratio (amplification factor) with that of the exact solution. It was concluded that UTOPIA contains all necessary cross-terms to third order and matches all terms in the Taylor expansion of the complex amplitude ratio.

Ekebjaerg and Justesen[19] introduced a nominally third-order, two-dimensional convection–diffusion scheme. They eliminated the truncation error terms arising from a lower-order scheme. The non-conservative scheme was then rewritten in a conservative pseudoflux difference form. The pseudofluxes chosen by Ekebjaerg and Justesen are not unique. Rasch[20] developed a third-order semi-

Lagrangian convection scheme in which he introduced weighting parameters to overcome the non-uniqueness problem. Rasch uses weighting parameters to generate a family of possible pseudoflux difference algorithms.

Recently, Leonard[21] has introduced a flux integral method (FIM) for multidimensional convection and diffusion. The convective-plus-diffusive flux at each face of a control volume cell is estimated by integrating the transported variable and its face-normal derivative over the volume swept out by the convecting velocity field. This gives a unique description of fluxes. The FIM has been applied to different schemes. The new version of UTOPIA (eight-point scheme) has been introduced by using the FIM as shown in Figure 2.

In this paper another convective scheme referred to as the skew third-order upwinding scheme (STOUS) is introduced. Unlike UTOPIA, STOUS uses a quadratic interpolation that is spatially skewed at the earlier time level to estimate the face value. The different interpolation points for UTOPIA and STOUS are compared in Figure 2. STOUS accurately estimates the face value of the control volume (CV) by following the space–time path of a fluid particle in choosing the interpolation points. The Fourier–von Neumann analysis shows that STOUS is nearly third-order accurate. STOUS is formulated in such a way that it is not explicitly dependent on the aspect ratio $\Delta x/\Delta y$; however, Δx and Δy are incorporated in the respective Courant numbers. Both UTOPIA and STOUS suffer from small oscillations which can be avoided by applying the universal limiter.[13] A rotating velocity field benchmark test is used to show the validity of STOUS and the results are compared with UTOPIA in Figure 6.

The main purpose of this paper is to introduce an algorithm with low numerical diffusion that can be used to simulate unsteady flows in general and the transport of dye in settling tanks in particular. As a first step the explicit third-order upwinding scheme (STOUS) is tested by solving the coupled non-linear equations of motion for turbulent recirculating flow in sedimentation tanks. This type of flow has been studied by many researchers with various types of numerical methods.[22–26] The effect of density currents on the flow in final clarifiers has been studied by Devantier and Larock[27], and Zhou and McCorquodale.[28] None of these studies used an explicit (Lagrangian) technique, although these schemes, which are based on the use of time–space characteristics, are very attractive from the fundamental point of view, since they closely mimic the transient convection process. Some researchers used semi-Lagrangian schemes which are non-conservative when applied to unsteady problems.

In this paper the flow in a primary rectangular sedimentation tank is predicted using the unsteady vorticity–streamfunction formulation. The convective and diffusive terms are modelled by third-order upwinding techniques. This scheme overcomes instability problems which arise when convection terms are prevalent and eliminates the need for very fine grids or first-order upwinding. The k–ϵ turbulence model is used to simulate turbulence. The computer code was tested for several grids with different aspect ratios and in all cases it converged to the same steady state solution.

The convection–diffusion equation is solved with third-order upwinding techniques to obtain flow-through curves (FTCs) which in turn can be used to evaluate the hydraulic efficiency of settling tanks. The simulation of FTCs requires the use of a technique with low numerical diffusion. Adams and Rodi[29] used the QUICK scheme to model the unsteady transport equation. The QUICK algorithm is based on the assumption of slow time variation. Owing to the $O(\Delta t)$ time truncation error, they had to use a very small time step. They did not report how they eliminated the oscillations. Szalai *et al.*[(30)] used the hybrid linear parabolic approximation (HLPA) together with a three-level fully implicit (TLFI) scheme. The degree of accuracy was restricted to second order. Finally, it should be pointed out that further research is under way, by the authors, to use the highly accurate third-order upwinding technique in general to simulate unsteady effects of density flows in sedimentation tanks.

2. NUMERICAL TECHNIQUES

Unsteady, two dimensional convection and diffusion of a scalar Φ are described by

$$\frac{\partial \Phi}{\partial t} = -\frac{\partial u\Phi}{\partial x} - \frac{\partial v\Phi}{\partial y} + \frac{\partial}{\partial x}\left(\Gamma_x \frac{\partial \Phi}{\partial x}\right) + \frac{\partial}{\partial y}\left(\Gamma_y \frac{\partial \Phi}{\partial y}\right) + S, \tag{2}$$

where u and v are the convection velocities, Γ_x and Γ_y are the diffusion coefficients in the x- and y-direction respectively and S is the source term. This equation can be integrated in time from t to $t + \Delta t$ and in space across the control volume cell (Figure 1) to yield

$$\frac{\bar{\Phi}_i^{n+1} - \bar{\Phi}_i^n}{\Delta t} = -\frac{(u\Phi)_e - (u\Phi)_w}{\Delta x} - \frac{(v\Phi)_n - (v\Phi)_s}{\Delta y} + \frac{(\Gamma_x \partial\Phi/\partial x)_e - (\Gamma_x \partial\Phi/\partial x)_w}{\Delta x} + \frac{(\Gamma_y \partial\Phi/\partial y)_n - (\Gamma_y \partial\Phi/\partial y)_s}{\Delta y} + \bar{S}^*, \tag{3}$$

in which the overbar represents the spatial average. The terms on the right-hand side of (3) are all time-averaged. The subscript notation is defined in Figure 1 and the superscript represents the time level.

2.1. Uniformly Third-Order Polynomial Interpolation Algorithm (UTOPIA)

Leonard and Niknafs[15] introduced this algorithm as an extension of the QUICKEST scheme.[6] The two dimensional scheme is based on the third-order polynomial expression

$$\phi^n = a + bx + cx^2 + dx^3 + ey + fy^2 + gy^3 + hxy + ix^2y + jxy^2, \tag{4}$$

requiring 10 collocation points. Using a square grid of unit size and following the west face stencil shown in Figure 2, the resulting formula for the west face value can be then written as

$$\Phi_w = \tfrac{1}{2}(\Phi_p + \Phi_w) - \frac{C_x}{2}\mathrm{GRADN} - \frac{1 - C_x^2}{6}\mathrm{CURVN} - \frac{C_y}{2}\mathrm{GRADT} + \left(\frac{C_y^2}{6} - \frac{C_y}{4}\right)\mathrm{CURVT} + \left(\frac{C_x C_y}{3} - \frac{C_y}{4}\right)\mathrm{TWIST}, \tag{5}$$

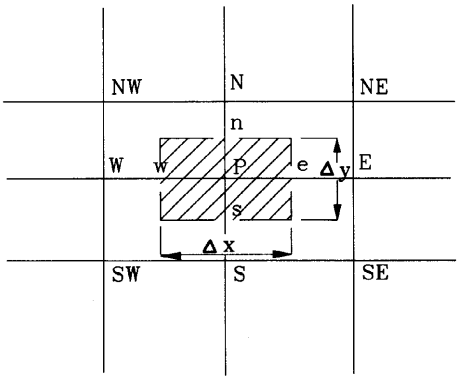

Figure 1. Control volume cell

where the x and y Courant numbers are

$$C_x = \frac{u\Delta t}{\Delta x}, \qquad C_y = \frac{v\Delta t}{\Delta y} \tag{6}$$

and

$$\begin{aligned}
\text{GRADN} &= \Phi_P - \Phi_{\text{W}},\\
\text{GRADT} &= \begin{cases} \Phi_{\text{W}} - \Phi_{\text{SW}} & \text{for } C_x > 0 \text{ and } C_y > 0,\\ \Phi_{\text{NW}} - \Phi_{\text{W}} & \text{for } C_x > 0 \text{ and } C_y < 0,\\ \Phi_{\text{P}} - \Phi_{\text{S}} & \text{for } C_x < 0 \text{ and } C_y > 0,\\ \Phi_{\text{N}} - \Phi_{\text{P}} & \text{for } C_x < 0 \text{ and } C_y < 0, \end{cases}\\
\text{CURVN} &= \begin{cases} \Phi_{\text{P}} - 2\Phi_{\text{W}} + \Phi_{\text{WW}} & \text{for } C_x > 0,\\ \Phi_{\text{E}} - 2\Phi_{\text{P}} + \Phi_{\text{W}} & \text{for } C_x < 0, \end{cases}\\
\text{CURVT} &= \begin{cases} \Phi_{\text{NW}} - 2\Phi_{\text{W}} = \Phi_{\text{SW}} & \text{for } C_x > 0,\\ \Phi_{\text{N}} - 2\Phi_{\text{P}} + \Phi_{\text{S}} & \text{for } C_x < 0, \end{cases}\\
\text{TWIST} &= \begin{cases} \Phi_{\text{P}} - \Phi_{\text{S}} - \Phi_{\text{W}} + \Phi_{\text{SW}} & \text{for } C_y > 0,\\ \Phi_{\text{N}} - \Phi_{\text{P}} - \Phi_{\text{NW}} + \Phi_{\text{W}} & \text{for } C_y < 0. \end{cases}
\end{aligned}$$

It is clear from the above expressions that the face value Φ_{w} should be modified to account for the aspect ratio $\Delta x/\Delta y$ if an arbitrary rectangular element is used. Using a convective estimate of the average face gradients, the corresponding face gradient is given by

$$\left(\frac{\partial \Phi}{\partial x}\right)_{\text{w}} = \frac{1}{\Delta x}\left(\text{GRADN} - \frac{C_x}{2}\text{CURVN} - \frac{C_y}{2}\text{TWIST}\right). \tag{7}$$

The latest version of UTOPIA with the FIM uses 12 collocation points with eight nodes per control volume face.[21]

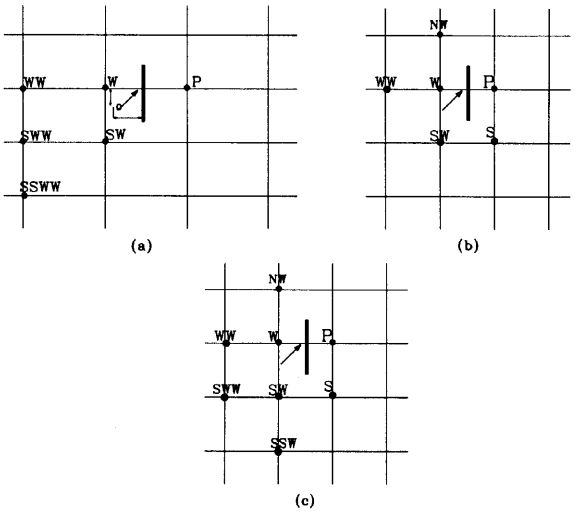

Figure 2. Computational stencil for $u, v > 0{\cdot}0$: (a) STOUS; (b) UTOPIA; (c) UTOPIA (flux integral method)

2.2. Skew Third Order Upwinding Scheme (STOUS)

In this algorithm the face value is determined by fixing a spatially skewed quadratic interpolation scheme among the points shown in Figure 2. The west face value for constant Δx and Δy is given by

$$\phi_w = N_P\phi_P + N_W\phi_W + N_{WW}\phi_{WW} + N_{SWW}\phi_{SWW} + N_{SW}\phi_{SW} + N_{SSWW}\phi_{SSWW}, \tag{8}$$

where N_K is the quadratic interpolation function (influence coefficient) of node K. All the interpolation functions should be evaluated at point O (origination point), which is the intersection with the t-plane of the time–space trajectory that passes through the centroid of the cell face. To locate point O, δx and δy can be calculated from

$$\delta x = \frac{u\Delta t}{2}, \qquad \delta y = \frac{v\Delta t}{2}. \tag{9}$$

Thus

$$\delta x = \frac{C_x\Delta x}{2}, \qquad \delta y = \frac{C_y\Delta y}{2}. \tag{10}$$

Evaluating the interpolation functions at point O and substituting into (7) (see Appendix I), the west face value becomes

$$\begin{aligned}\Phi_w = {} & \tfrac{1}{8}(3\phi_P - \Phi_{WW} + 6\Phi_W) + \frac{C_x}{2}(\Phi_W - \Phi_P) + \frac{C_y}{4}(3\Phi_{SW} - \Phi_{SSWW} + \Phi_{SWW} - 3\Phi_W) \\ & + \frac{C_x^2}{8}(\Phi_P - 2\Phi_W + \Phi_{WW}) + \frac{C_y^2}{8}(\Phi_{SSWW} - 2\Phi_{SWW} + \Phi_{WW}) + \frac{C_xC_y}{4}(\Phi_{SWW} - \Phi_{WW} - \Phi_{SW} + \Phi_W),\end{aligned} \tag{11}$$

which can be written in a similar form to (5) as

$$\begin{aligned}\Phi_w = {} & \tfrac{1}{2}(\Phi_P + \Phi_W) - \frac{C_x}{2}\mathrm{GRADN} - \frac{1 - C_x^2}{8}\mathrm{CURVN} - \frac{C_y}{2}\mathrm{GRADT} + \left(\frac{C_y^2}{8} - \frac{|C_y|}{4}\right)\mathrm{CURVTS} \\ & + \left(\frac{|C_xC_y|}{4} - \frac{|C_y|}{4}\right)\mathrm{TWISTS},\end{aligned} \tag{12}$$

where CURVTS and TWISTS refer to the skew transversal curvature and skew twist terms respectively. They depend on the direction of the velocity vector at the cell face as given in Appendix I. The factor $\frac{1}{8}$ (rather than $\frac{1}{6}$) comes from the use of nodal values and not from cell averages. Following Leonard[15,31] and introducing the physical diffusion contribution in estimating the face value, the west face value can be written as

$$\begin{aligned}\Phi_w = {} & \tfrac{1}{2}(\Phi_P + \Phi_W) - \frac{C_x}{2}\mathrm{GRADN} - \left(\frac{1}{8} - \frac{C_x^2}{8} - \frac{\alpha_x}{2}\right)\mathrm{CURVN} - \frac{C_y}{2}\mathrm{GRADT} \\ & + \left(\frac{C_y^2}{8} - \frac{|C_y|}{4} + \frac{\alpha_y}{2}\right)\mathrm{CURVTS} + \left(\frac{|C_xC_y|}{4} - \frac{|C_y|}{4}\right)\mathrm{TWISTS},\end{aligned} \tag{13}$$

where

$$\alpha_x = \Gamma_x\frac{\Delta t}{\Delta x^2}, \qquad \alpha_y = \Gamma_y\frac{\Delta t}{\Delta y^2}. \tag{14}$$

The STOUS face gradient is given by

$$\left(\frac{\partial\Phi}{\partial x}\right)_{\mathrm{W}} = \frac{1}{\Delta x}\left(\mathrm{GRADN} - \frac{C_x}{2}\mathrm{CURVN} - \frac{C_y}{2}\mathrm{TWIST}\right). \tag{15}$$

STOUS uses 11 collocation points with seven nodes per control volume face.

2.3. Stability analysis of STOUS and UTOPIA

The von Neumann stability analysis has been applied to both STOUS and UTOPIA. In this analysis the Fourier component of the solution is defined as

$$\Phi_{i,j}^{n} = V^{n}\mathrm{e}^{I(i\theta_x + j\theta_y)}, \tag{16}$$

where V^n is the amplitude function at time level n of the particular component whose phase angles are defined as $\theta_x = K_x\Delta x$ and $\theta_y = K_y\Delta y$, where K_x and K_y are the wave numbers. The Fourier components at different points are given in Appendix II where it is shown that the STOUS amplification factor can be given as

$$G_{\mathrm{STOUS}} = R_{\mathrm{SC}x} + R_{\mathrm{SC}y} + R_{\mathrm{SD}x} + R_{\mathrm{SD}y} + I_{\mathrm{SC}x} + I_{\mathrm{SC}y} + I_{\mathrm{SD}x} + I_{\mathrm{SD}y}, \tag{17}$$

where $R_{\mathrm{SC}x}$, and $R_{\mathrm{SC}y}$, represent the real parts of the STOUS advective terms in the x- and y-direction respectively, $R_{\mathrm{SD}x}$, and $R_{\mathrm{SD}y}$ represent the real parts of the STOUS diffusion terms in the x- and y-direction respectively and $I_{\mathrm{SC}x}$, $I_{\mathrm{SC}y}$, $I_{\mathrm{SD}x}$, and $I_{\mathrm{SD}y}$ represent the imaginary parts of the corresponding terms. These terms are as follows (details are given in Appendix II):

$$\begin{aligned}
R_{\mathrm{SC}x} = {} & \frac{C_x^2}{2}(2\cos\theta_x - 2) - \left(\frac{C_x}{8} - \frac{C_x^3}{8} - \alpha\frac{C_x}{2}\right)[2(1-\cos\theta_x)^2] - \frac{C_xC_y}{2}(1 - \cos\theta_y - \cos\theta_x \\
& + \cos\theta_x\cos\theta_y + \sin\theta_x\sin\theta_y) - \left(\frac{C_y^2C_x}{8} - \frac{C_yC_x}{4} + \alpha\frac{C_x}{2}\right)(\cos 2\theta_y\cos\theta_x - \sin 2\theta_y\sin\theta_x \\
& - 2\cos\theta_y\cos\theta_x + 2\sin\theta_y\sin\theta_x + \cos\theta_x - \cos 2\theta_y\sin 2\theta_y + \sin 2\theta_y\sin 2\theta_x \\
& + 2\cos\theta_y\cos 2\theta_x - 2\sin\theta_y\sin 2\theta_x - \cos 2\theta_x) - \left(\frac{C_x^2C_y}{4} - \frac{C_xC_y}{4}\right)(2\cos\theta_y\cos\theta_x \\
& + 2\sin\theta_y\sin\theta_x - 2\cos\theta_x - \cos\theta_y - \cos\theta_y\cos 2\theta_x - \sin\theta_y\sin\theta_x + \cos 2\theta_x),
\end{aligned} \tag{18}$$

$$\begin{aligned}
I_{\mathrm{SC}x} = {} & I\Bigg[-C_x\sin\theta_x + \left(\frac{C_x}{8} - \frac{C_x^3}{8} - \alpha\frac{C_x}{2}\right)(\sin 2\theta_x - 2\sin\theta_x) + \frac{C_xC_y}{2}(\sin\theta_x - \sin\theta_y\cos\theta_x \\
& - \sin\theta_x\cos\theta_y) + \left(\frac{C_y^2C_x}{8} - \frac{C_yC_x}{4} + \alpha\frac{C_x}{2}\right)(\sin 2\theta_y\cos\theta_x + \cos 2\theta_y\sin\theta_x - 2\sin\theta_y\cos\theta_x \\
& - 2\sin\theta_x\cos\theta_y + \sin\theta_x - \sin 2\theta_y\cos 2\theta_x - \sin 2\theta_x\cos 2\theta_y + 2\sin\theta_y\cos 2\theta_x \\
& + 2\sin\theta_x\cos\theta_y - \sin 2\theta_x) + \left(\frac{C_x^2C_y}{4} - \frac{C_yC_x}{4}\right)(2\sin\theta_y\cos\theta_x + 2\sin\theta_x\cos\theta_y - 2\sin\theta_x \\
& - \sin\theta_y - \sin\theta_y\cos 2\theta_x - \sin 2\theta_x\cos\theta_y + \sin 2\theta_x)\Bigg]
\end{aligned} \tag{19}$$

$$R_{\mathrm{SD}x} = \alpha\left(2\cos\theta_x - 2 + \frac{C_x}{2}[2(1-\cos\theta_x)^2] - \frac{C_y}{2}(2\cos\theta_x - 2\cos\theta_x\cos\theta_y - 2 + 2\cos\theta_y)\right), \tag{20}$$

$$I_{\mathrm{SD}x} = I\alpha\left(\frac{C_x}{2}(2\sin\theta_x - \sin 2\theta_x) + \frac{C_y}{2}(2\sin\theta_y\cos\theta_x - 2\sin\theta_y)\right), \tag{21}$$

with similar expressions for the y-direction.

The UTOPIA amplification factor is

$$G_{\mathrm{UTOPIA}} = R_{\mathrm{UC}x} + R_{\mathrm{UC}y} + R_{\mathrm{UD}x} + R_{\mathrm{UD}y} + R_{\mathrm{UC}x} + I_{\mathrm{UD}y} + I_{\mathrm{UD}x} + I_{\mathrm{UD}y}, \tag{22}$$

where

$$\begin{aligned} R_{\mathrm{UC}x} = {} & \frac{C_x^2}{2}(2\cos\theta_x - 2) - \left(\frac{C_x}{6} - \frac{C_x^3}{6} - \alpha\frac{C_x}{2}\right)[2(1-\cos\theta_x)^2] \\ & + \frac{C_xC_y}{2}(1 - \cos\theta_y - \cos\theta_x + \cos\theta_x\cos\theta_y + \sin\theta_x\sin\theta_y) \\ & - \left(\frac{C_y^2C_x}{6} - \frac{C_yC_x}{4} + \alpha\frac{C_x}{2}\right)(2\cos\theta_y - 2 - 2\cos\theta_y\cos\theta_x + 2\cos\theta_x) \\ & - \left(\frac{C_x^2C_y}{3} - \frac{C_xC_y}{4}\right)(2\cos\theta_x - 2\cos\theta_x\cos\theta_y - 2 + 2\cos\theta_y), \end{aligned} \tag{23}$$

$$\begin{aligned} I_{\mathrm{UC}x} = I\Bigg[& -C_x\sin\theta_x + \left(\frac{C_x}{6} - \frac{C_x^3}{6} - \alpha\frac{C_x}{2}\right)(\sin 2\theta_x - 2\sin\theta_x) \\ & + \frac{C_xC_y}{2}(\sin\theta_x - \sin\theta_y\cos\theta_x - \sin\theta_x\cos\theta_y) \\ & - \left(\frac{C_y^2C_x}{6} - \frac{C_yC_x}{4} + \alpha\frac{C_x}{2}\right)(2\cos\theta_y - 2\sin\theta_x) \\ & - \left(\frac{C_x^2C_y}{3} - \frac{C_yC_x}{4}\right)(2\sin\theta_y\cos\theta_x - 2\sin\theta_y)\Bigg]. \end{aligned} \tag{24}$$

The real and imaginary parts of the UTOPIA diffusion terms, $R_{\mathrm{UD}x}$, $R_{\mathrm{UD}y}$, $I_{\mathrm{UD}x}$, and $I_{\mathrm{UD}y}$, are the same as the STOUS terms, since both STOUS and UTOPIA have the same face gradient expression.

By parametric scanning over a wide range of values of α, C_x and C_y, the complete stability region ($G < 1$) for STOUS and UTOPIA was found as shown in Figures 3(a)–3(d). It is evident that in STOUS the stability range is considerably wider than in UTOPIA. Figure 4(a) shows the stability range for the case $C_x = C_y$; the maximum Courant number for STOUS is 0·5 compared with 0·25 for UTOPIA. Figure 4(b) shows another case ($C_x = 0{\cdot}2$) in which the maximum C_y is also higher for STOUS than for UTOPIA. Figure 4(c) compares STOUS and UTOPIA for the case of pure advection, i.e. $\alpha = 0{\cdot}0$ ($Pe = \infty$), and indicates that STOUS has a wider stability range in this case. The cross-term C_xC_y is the main reason for the stability of STOUS and UTOPIA; the schemes such as the componentwise application of the 1D algorithms without this term are unstable.

Both UTOPIA and STOUS suffer from numerical oscillations at a sharp gradient. Although STOUS produces very small oscillations (about 5%) compared with other schemes, it is still important to eliminate these oscillations, especially when solving the non-linear equations of motion. A well-developed bounding technique known as the universal limiter (UL) is used to avoid these oscillations (Figure 5) Details of the universal limiter can be found elsewhere;[13,15] however, the following brief description of the procedure is given.

(i) For each face, based on the direction of the normal velocity, the values ϕ_{U} (upstream point), ϕ_{c} (cell) and ϕ_{D} (downstream point) are identified.
(ii) The face values are determined by STOUS (or UTOPIA).

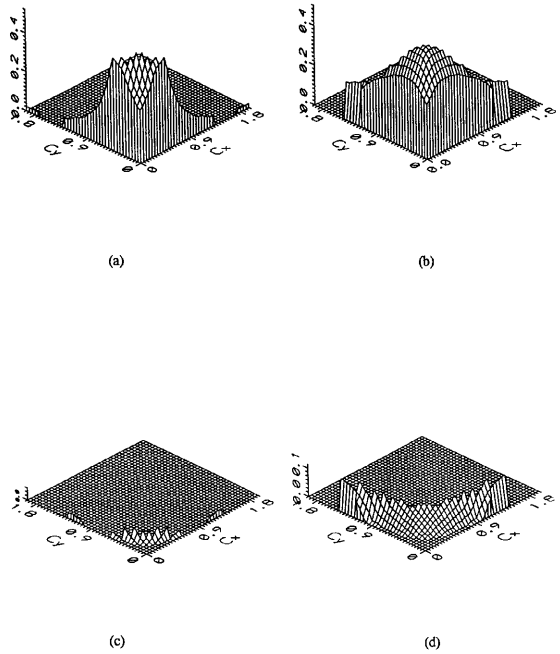

Figure 3. Stability range: (a) UTOPIA (max α); (b) STOUS (max α); (c) UTOPIA (min α); (d) STOUS (min α)

(iii) The normalized face and cell values are computed by

$$\bar{\phi} = \frac{\phi - \phi_{\mathrm{U}}}{\phi_{\mathrm{D}} - \phi_{\mathrm{U}}}. \tag{25}$$

(iv) If the point $(\phi_{\mathrm{C}}, \phi_{\mathrm{f}})$ falls within the triangular region of Figure 5, then the computation proceeds to the next CV face.

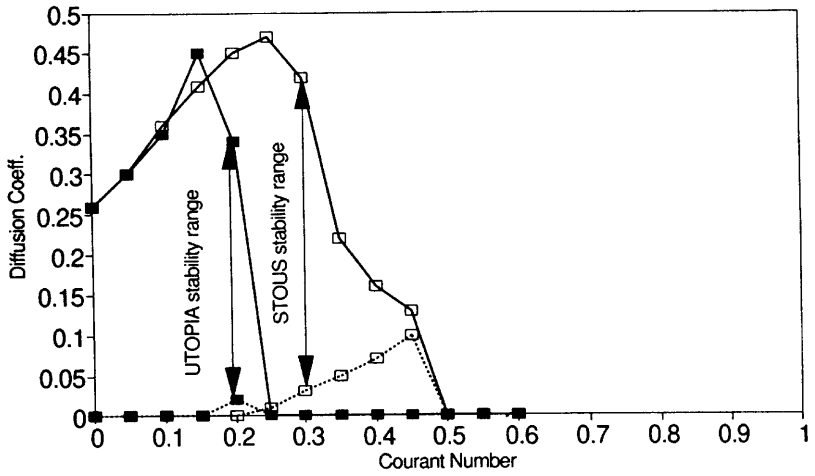

Figure 4(a). Comparison between UTOPIA and STOUS for $C_x = C_y$: —■—, UTOPIA (max α); - -■- -, UTOPIA (min α); —⊟—, STOUS (max α); - -⊡- -, STOUS (min α)

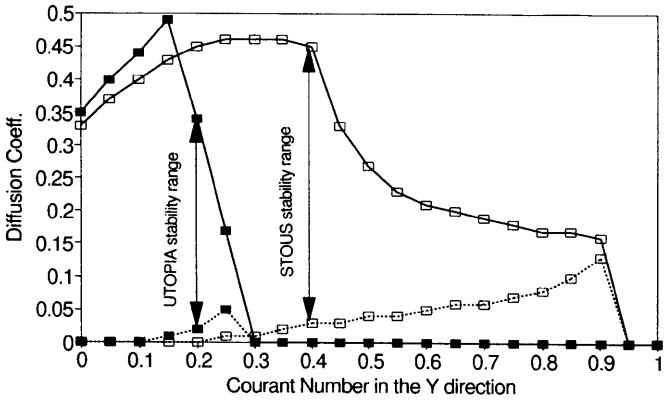

Figure 4(b). Comparison betweemn UTOPIA and STOUS for $C_x = 0{\cdot}2$: —■— , UTOPIA (max α); - -■- -, UTOPIA (min); —⊟— , STOUS (max α); - -⊡- -, STOUS (min α)

(v) If not, ϕ_v is limited to the nearest appropriate constraint boundary at the given ϕ_c-value.
(vi) The unnormalized face values are determined.

A 1D adaptive discriminator is used in each direction to avoid clipping narrow extrema,[3] this can identify well-defined local narrow physical extrema and automatically switch off the universal limiter, but keep it in regions where unphysical overshoots would otherwise occur.

2.4. Benchmark test problem

The rotating velocity field problem is used as a benchmark test. For pure convection the exact solution is known. As an initial condition a cylinder with a base diameter of 40% of the domain width is used. The computation was carried out on meshes ranging from 30×30 to 70×70 for a half-rotation in the counter clockwise direction. First-order upwinding, STOUS and UTOPIA were used in

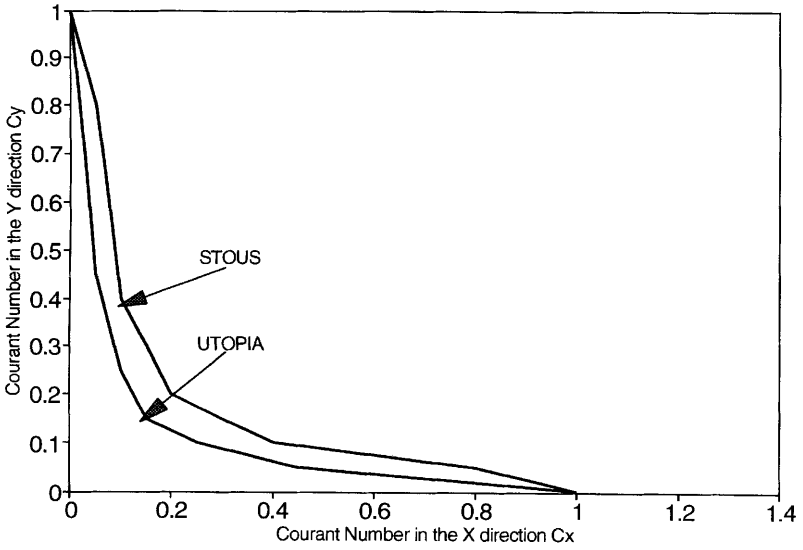

Figure 4(c). Comparison between UTOPIA and STOUS for pure advection ($Pe = \infty$)

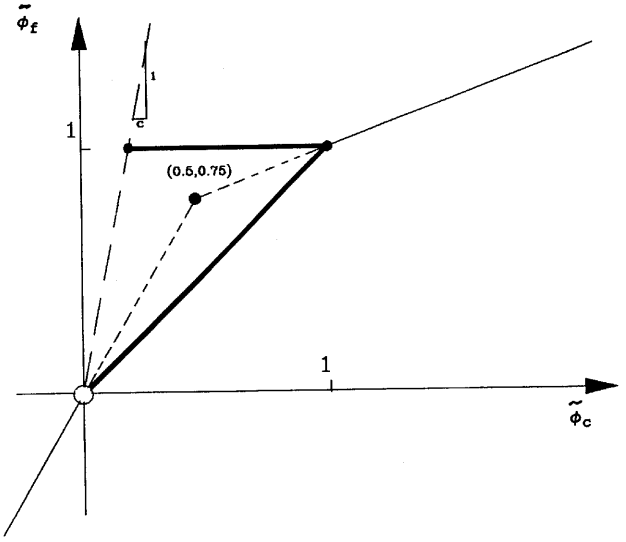

Figure 5. Universal limiter (UL) constraints in normalized variable diagram (NVD)

this test problem. For the first-order upwinding scheme the alternate direction implicit (ADI) technique was used so that the maximum Courant number and thus the least CPU time could be obtained. For each grid, multiple trials were made to determine the maximum allowable Courant number after which instability problems occurred. Explicit algorithms were used for STOUS and UTOPIA. It was found that the maximum Courant number for STOUS (1·0–1·2) is greater than for UTOPIA (0·8–0·9). Table I gives the computed maximum Courant numbers for each technique, the absolute errors and the CPU times in minutes on a Pentium-90 PC. Figures 6(a)–6(d) show the first-order upwinding, STOUS and UTOPIA predictions and the analytical solution for a grid of 70 × 70. Figure 7 shows the cost (CPU time) versus the absolute error, which is defined as

$$e = \sum_i \sum_j \frac{|\phi_{\text{comp}} - \phi_{\text{exact}}|}{\text{Number of grid points}}. \tag{26}$$

Table I. Comparison between rirst-order upwinding, STOUS and UTOPIA

Mesh	First-order upwinding $C_{\max} = 1{\cdot}5-1{\cdot}7$		STOUS $C_{\max} = 1{\cdot}0$		UTOPIA $C_{\max} = 0{\cdot}875$	
	e	$T_{\min}$	e	$T_{\min}$	e	$T_{\min}$
30 × 30	0·0732	3·2	0·0268	4·5	0·0262	5·5
35 × 35	0·0647	7·2	0·0232	10	0·0226	12
40 × 40	0·0576	15	0·0201	19	0·0196	24
45 × 45	0·0547	26	0·0184	34	0·0180	42
50 × 50	0·0518	45	0·0172	62	0·0157	70
55 × 55	0·0503	56	0·0162	99	0·0157	106
60 × 60	0·0460	82	0·0149	152	0·0143	164
70 × 70	0·0403	213	0·0130	300	0·0125	341

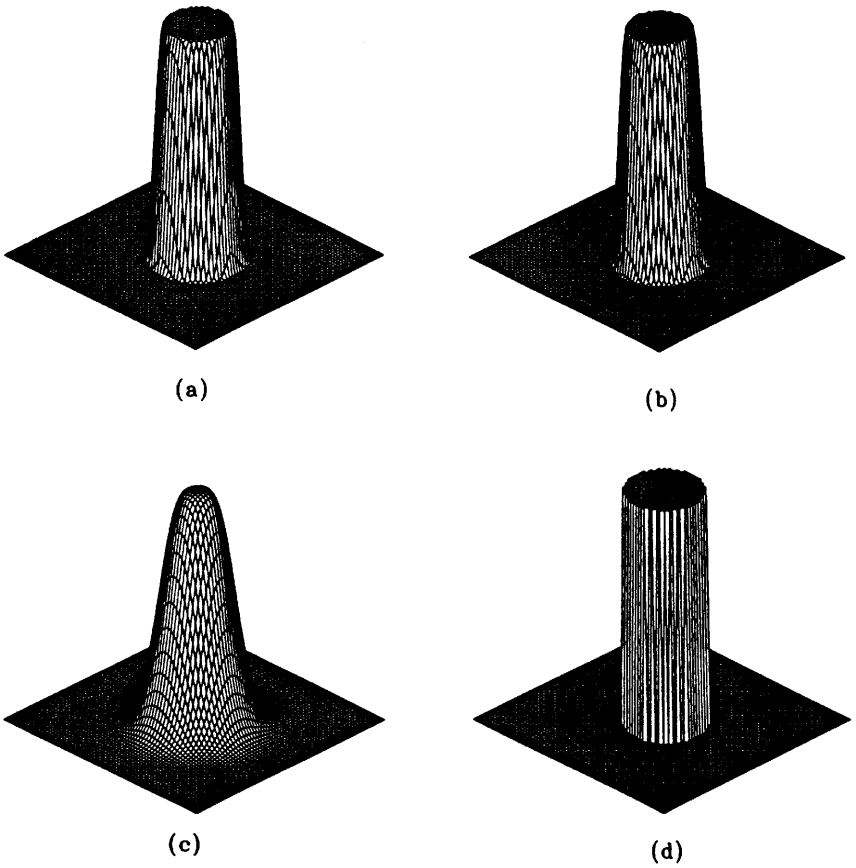

Figure 6. Rotating velocity test problem for a grid of 70 × 70: (a) UTOPIA ($C = 0{\cdot}875$); (b) STOUS ($C = 1{\cdot}0$); (c) first-order upwinding ($C = 1{\cdot}5$); (d) exact solution

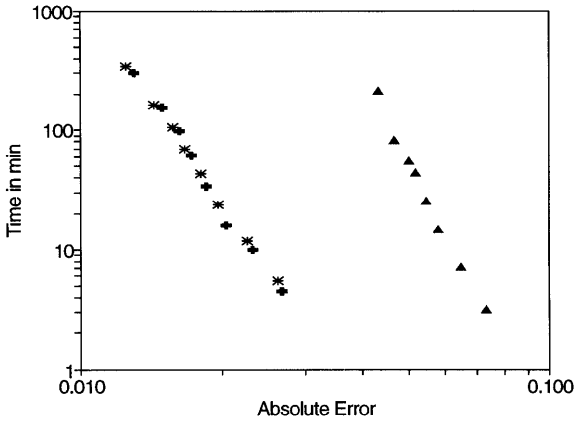

Figure 7. Cost (CPU time)–absolute error relation: ▲, HYBRID; ∗, STOUS; +, UTOPIA

It is clear from Figure 7 that both STOUS and UTOPIA give much better accuracy (less absolute error) for the same cost (CPU time) compared with first-order upwinding.

3. SETTLING TANK MODEL

3.1. General equations

The equations describing a two-dimensional, unsteady, turbulent flow in a rectangular sedimentation basin are

$$\frac{\partial u^*}{\partial x^*} + \frac{\partial v^*}{\partial y^*} = 0, \tag{27}$$

$$\frac{\partial u^*}{\partial t^*} + u^* \frac{\partial u^*}{\partial x^*} + v^* \frac{\partial u^*}{\partial y^*} = -\frac{1}{\rho^*}\frac{\partial p^*}{\partial x^*} + \frac{\partial}{\partial x^*}\left(\nu_t^* \frac{\partial u^*}{\partial x^*}\right) + \frac{\partial}{\partial y^*}\left(\nu_t^* \frac{\partial u^*}{\partial y^*}\right) + S_y^*, \tag{28}$$

$$\frac{\partial v^*}{\partial t^*} + u^* \frac{\partial v^*}{\partial x^*} + v^* \frac{\partial v^*}{\partial y^*} = -\frac{1}{\rho^*}\frac{\partial p^*}{\partial x^*} + \frac{\partial}{\partial x^*}\left(\nu_t^* \frac{\partial v^*}{\partial x^*}\right) + \frac{\partial}{\partial y^*}\left(\nu_t^* \frac{\partial v^*}{\partial y^*}\right) + F_g^* + S_v^*, \tag{29}$$

in which u^* and v^* are the horizontal and vertical mean velocity components respectively, ρ^* is the fluid density, ν_t^* is the eddy viscosity and p^* is the pressure. F_g^* represents the body force (gravitational force). Since the eddy viscosity ν_t^* is not constant, the two source terms S_u^* and S_v^* do not vanish on application of the continuity equation.[28] The superscript asterisks in (27)–(29) denote dimensional quantities. Using the relationships

$$u^* = \frac{\partial \psi^*}{\partial y^*}, \qquad v^* = -\frac{\partial \psi^*}{\partial x^*}, \qquad \omega^* = \frac{\partial u^*}{\partial y^*} - \frac{\partial v^*}{\partial x^*}, \tag{30}$$

where ψ^* is the streamfunction and ω^* is the vorticity, equation (27)–(30) can be replaced by the equations

$$\frac{\partial \omega^*}{\partial t^*} + \frac{\partial u^* \omega^*}{\partial x^*} + \frac{\partial v^* \omega^*}{\partial y^*} = \frac{\partial}{\partial x^*}\left(\nu_t{}^* \frac{\partial \omega}{\partial x^*}\right) + \frac{\partial}{\partial y^*}\left(\nu_t^* \frac{\partial \omega^*}{\partial y^*}\right) + S_\omega^*, \tag{31}$$

$$\nabla^2 \psi^* = \omega^* \tag{32}$$

or, in non-dimensional form,

$$\frac{\partial \omega}{\partial t} + \frac{\partial u\omega}{\partial x} + \frac{\partial v\omega}{\partial y} = \frac{\partial}{\partial x}\left(\nu_t \frac{\partial \omega}{\partial x}\right) + \frac{\partial}{\partial y}\left(\nu_t \frac{\partial \omega}{\partial y}\right) + S_\omega, \tag{33}$$

$$\nabla^2 \psi = \omega, \tag{34}$$

in which $u = u^*/U, v = v^*/U, \quad x = x^*/H, \quad y = y^*/H, t = t^*/(H/U), \quad \nu_t = \nu_t^*/UH = Re_t^{-1}$, $\psi = \psi^*/UH$ and $\omega = \omega^*/(U/H)$. The characteristic velocity and length scales U and H are selected to be convective scales, i.e. the depth-averaged longitudinal velocity and the tank depth respectively.

3.2. Laminar flow past a backward-facing step

A benchmark test problem of flow over a backward-facing step was used to check the implementation of the streamfunction–vorticity formulation. Equations (31)–(32) can be used to describe the two-dimensional laminar flow after replacing the eddy viscosity by the molecular

kinematic viscosity of water. The no slip boundary condition was used for the upper and lower walls. A fully developed velocity distribution was used at the inlet. The outlet boundary condition was $\partial u/\partial x = 0$. The solution starts by assigning initial values for ψ and ω. A typical computational cycle begins by using equation (31) to advance the solution of ω^n to $t + \Delta t$. The SOR method is used to find the new ψ^{n+1} at all points from the differenced form of (32), using the new ω^{n+1} at the interior points as the source term. The velocity components are updated by substituting the ψ^{n+1}-values in (30). Finally, vorticity values ω^{n+1} are calculated for boundary nodes. The second-order-accurate boundary condition for vorticity along a no-slip wall is used. This boundary condition is

$$\omega_N = \frac{3\omega_{N-1} - \omega_N}{\Delta n^2} - \tfrac{1}{2}\omega_{N+1}, \tag{35}$$

where N and $N - 1$ denote quantities evaluated at the wall and one point in from the wall respectively and Δn is the normal distance between N and $N - 1$. The computational cycle is repeated until the specified convergence criterion for a steady state is satisfied. An expansion ratio E (ratio of step height to inlet channel height) of 0·5 was used with Reynolds number $Re = 200$ (based on the average inlet velocity and twice the inlet channel height). The predicted velocity distribution is shown in Figure 8(a) shows good agreement between the STOUS velocity distribution and experimental data of Armaly *et al.*[32]

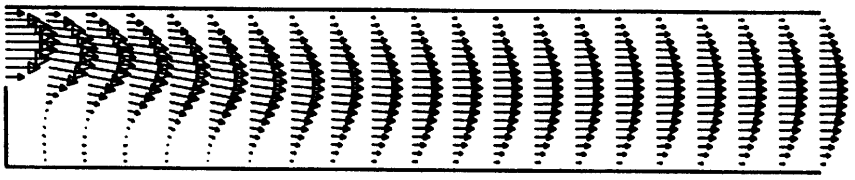

Figure 8(a). Velocity field for backward-facing step

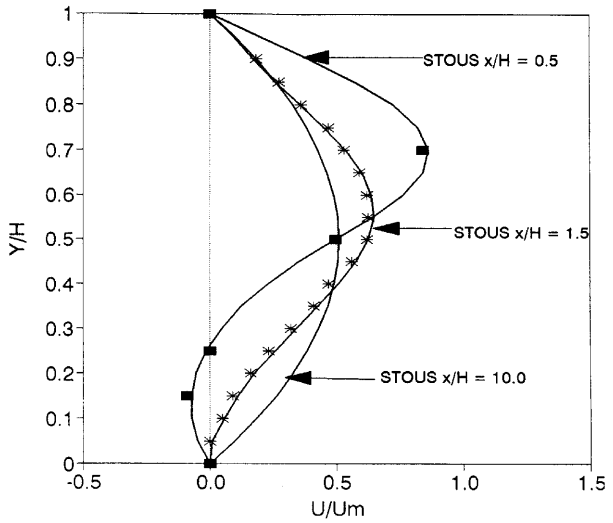

Figure 8(b). Velocity profiles at various locations: ■, Thangam; ∗, experimental data of Armaly *et al.*[32]

3.3. Turbulence model

The eddy viscosity coefficient is related to the turbulent kinetic energy k and its rate of dissipation ϵ by

$$\nu_t = \frac{c_\mu k^2}{\epsilon}. \tag{36}$$

The variables k and ϵ, are computed from the transport equations[33]

$$\frac{\partial k}{\partial t} + u\frac{\partial k}{\partial x} + v\frac{\partial k}{\partial y} = \frac{\partial}{\partial x}\left(\frac{\nu_t}{\sigma_k}\frac{\partial k}{\partial x}\right) + \frac{\partial}{\partial y}\left(\frac{\nu_t}{\sigma_k}\frac{\partial k}{\partial y}\right) + P - \epsilon, \tag{37}$$

$$\frac{\partial \epsilon}{\partial t} + u\frac{\partial \epsilon}{\partial x} + v\frac{\partial \epsilon}{\partial y} = \frac{\partial}{\partial x}\left(\frac{\nu_t}{\sigma_\epsilon}\frac{\partial \epsilon}{\partial x}\right) + \frac{\partial}{\partial y}\left(\frac{\nu_t}{\sigma_\epsilon}\frac{\partial \epsilon}{\partial y}\right) + c_{\epsilon 1}\frac{\epsilon}{k}P - c_{\epsilon 2}\frac{\epsilon^2}{k}, \tag{38}$$

where P, the turbulent kinetic energy production, is given by

$$P = \nu_t\left[2\left(\frac{\partial u}{\partial x}\right)^2 + 2\left(\frac{\partial v}{\partial y}\right)^2 + \left(\frac{\partial u}{\partial y} + \frac{\partial v}{\partial x}\right)^2\right] \tag{39}$$

and which $c_\mu, c_{\epsilon 1}, c_{\epsilon 2}, c_{\epsilon 2}, \sigma_k$ and σ_ϵ have the values 0·09, 1·44, 1·92, 1·0, and 1·3 respectively.[33] Variables appearing in (36)–(39) are non-dimensional such that $k^* = kU^2$ and $\epsilon^* = \epsilon U^3/H$. The k and ϵ advection terms have been modelled by STOUS. Equations (33)–(34) and (36)–(38) represent a closed system of equations relating ω, ψ, k and ϵ.

An unsteady dye concentration equation is solved to obtain the FTC corresponding to the converged steady state velocity field:

$$\frac{\partial C}{\partial t} + \frac{\partial uC}{\partial x} + \frac{\partial vC}{\partial y} = \frac{\partial}{\partial x}\left(\Gamma_t\frac{\partial C}{\partial x}\right) + \frac{\partial}{\partial y}\left(\Gamma_t\frac{\partial C}{\partial y}\right), \tag{40}$$

in which Γ_t is the turbulent mass diffusivity which is assumed to be proportional to the eddy viscosity, i.e. $\Gamma_t = \nu_t/\sigma_c$, where σ_c is the turbulent Schmidt number.

3.4. Boundary conditions

3.4.1. Inlet boundary. Figure 9 shows the flow domain and associated boundaries. An experimentally determined, three-zone parabolic profile of the horizontal velocity is imposed along B1.[23] The vorticity is obtained by differentiating the velocity distribution, while the streamfunction is

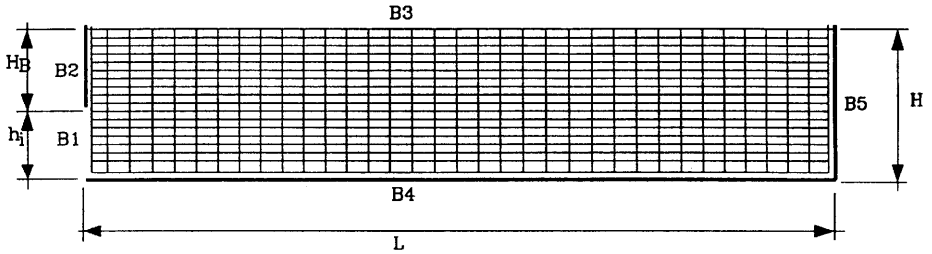

Figure 9. Defining sketch and boundary conditions for 17 × 34 mesh

calculated by integrating the velocity over B1. The inlet boundary conditions for the k–ϵ model were[25]

$$k = \alpha_k \frac{U_0^2}{U^2}, \qquad \epsilon = c_\mu^{3/4} \frac{k^{3/2}}{l_\mathrm{m}}, \tag{41}$$

in which $U_0 = q/h_\mathrm{i}$ and $l_m = 0{\cdot}5 c_\mu h_\mathrm{i}/H$, where q is the flow discharge per unit width and h_i is the baffle opening (Figure 9). $\alpha_k = 0{\cdot}2$ in this study owing to the presence of the upstream baffles which caused the incoming flow to be highly turbulent.[25] For typical inlet conditions, α_k is in the range 0·.05–0·1. The transient dye inlet boundary condition was set to $C = C_\mathrm{i}$ and held held at this value for a time corresponding to the dye injection time; thereafter $C = 0{\cdot}0$.

An external node is required for STOUS to be applied at B1; locally one-dimensional quadratic behaviour for ψ is assumed normal to the inlet, which implies that the vorticity gradient $\partial\omega/\partial x = 0$. This does not affect the accuracy of the flow field computations, because the vorticity at the inlet is mainly transported by advection owing to the high inlet velocity. This is achieved by setting

$$\phi_{N+1} = \phi_N, \tag{42}$$

where ϕ_{N+1} and ϕ_N are the external and boundary points respectively. At the corner the point SSWW can be taken as an average of the two adjacent points SWW and SSW.

3.4.2. Free surface boundary. The rigid lid approximation was applied with the normal gradients of k, ϵ, C and v set to zero. The full-slip condition is used, i.e. u is free to develop and $\Psi = 1{\cdot}0$ (excluding the sink point). In the absence of applied shear, such as wind shear and temperature gradients, $\omega = 0{\cdot}0$ (excluding the sink point).

3.4.3. Wall boundary. Along the inlet baffle B2, $\psi = 1{\cdot}0$; along the bottom B4 and the end wall B5 (excluding the sink point), $\psi = 0{\cdot}0$. The wall function approach was used to determine ψ, k and ϵ. In this approach the mesh does not extend all the way to the wall, because the turbulence model is only valid in the fully turbulent regime zone. Therefore the computational domain is shifted a small distance y_n from the wall (Figure 9). The friction velocity U_p^* at a point P (the first grid point from the wall) can be calculated from

$$\frac{U_\mathrm{P}}{U_\mathrm{P}^*} = \frac{1}{\kappa} \ln(E y_\mathrm{n}^+), \tag{43}$$

in which U_p is the parallel velocity at P, $y_\mathrm{n}^+ = y_\mathrm{n} U_\mathrm{p}^*/v$, and E is the roughness parameter which was taken as 9·8, and κ is the von Karman constant (0·42). At the interface the shear stress based on the outer flow domain is matched with the wall shear stress in the boundary layer. Thus for the bottom of the tank the vorticity at the edge of the near wall region is given by

$$\omega_\mathrm{w}^* = \frac{U_\mathrm{P}^{*2}}{v_\mathrm{tP}^*}, \tag{44}$$

in which ω_w^* is the dimensional wall vorticity. Both quadratic and cubic extrapolations of ψ normal to the boundary were examined to calculate the external node at the bottom. For the cubic extrapolation (Figure 10), the vorticity gradient is given by

$$\left(\frac{\partial\omega}{\partial y}\right)_N = \frac{\omega_{N+1/2} - \omega_{N-1/2}}{\Delta y}, \tag{45}$$

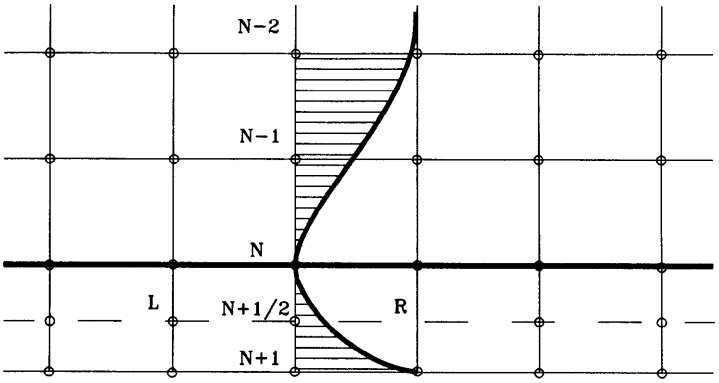

Figure 10. STOUS boundary conditions showing cubic extrapolation of Ψ using internal node values

where

$$\omega_{N+1/2} = \frac{\psi_{\mathrm{R}} - 2\psi_{N+1/2} + \psi_{\mathrm{L}}}{\Delta x^2} + \frac{\psi_N - 2\psi_{N+1/2} + \psi_{N+1}}{\Delta y^2}, \tag{46}$$

and thus the external node can be calculated as

$$\omega_{N+1} = \omega_N + \Delta y \left(\frac{\partial \omega}{\partial y}\right)_N. \tag{47}$$

No significant difference in the velocity field was indicated when the two types of boundary conditions were compared. This could be due to the boundary condition used, i.e. the eddy viscosity at the bottom of the tank as predicted by the k–ϵ model. For the k–= turbulence model the kinetic energy production is assumed to be equal to the dissipation rate near the boundaries. The boundary conditions for k and ϵ become[34]

$$k = \frac{U_{\mathrm{P}}^{*2}}{\sqrt{c_\mu}}, \qquad \epsilon = \frac{U_{\mathrm{P}}^{*3}}{\kappa y_{\mathrm{n}}}. \tag{48}$$

A more general treatment can also be used in which k is determined by a balance of diffusion, convection, production and dissipation for near-wall control volumes.[35] Assuming a zero-gradient boundary condition, an external node is computed and thus STOUS can be applied. For the dye transport equation the zero-flux boundary condition is used, i.e $\partial C/\partial N = 0{\cdot}0$.

3.4.4. Outlet boundary. The normal gradients of k, ϵ, and C were set to zero at the outlet.[29] The approach of Imam and McCorquodale[23] is used for the boundary conditions of ω and ψ.

3.4.5. Initial conditions. An irrotational flow solution of (34), i.e. $\omega = 0{\cdot}0$, is used for the initial values of ψ and thus the velocity components u and v are obtained at the internal nodes using (30). The initial values for k and ϵ are not crucial as long as the unsteady flow equations are solved until steady state is reached. For the transient dye simulation the concentration of the dye was set to zero.

3.5. Grid independence test

Various grids have been used to check the grid convergence. The maximum streamfunction at the centre of the recirculating zone (ψ_c) was used to check the grid convergence. A relatively short settling tank ($L/H = 2$) was used to test a wide range of mesh sizes. Figure 11 shows the effect of the mesh size on ψ_c; it is evident that as the mesh Δx diminishes, ψ_c converges in the limit to 1·095. Because of non-linearities inherent in the UL, the time step was chosen so that the maximum Courant number would not exceed 0·3.[36] No significant difference was found in the flow patterns for the grids tested.

3.6. Application of model

The model was applied to simulate the hydrodynamics and dye concentration fields in rectangular tanks studied experimentally by Imam.[37](37). Figure 12 shows two velocity fields for two flow situations using two different grids. In the first case the flow rate was 45·2 $cm^3\ s^{-1}\ cm^{-1}$. The comparison between the measured and predicted fields is shown in Figure 13. The inlet velocity is assumed to follow the three zone inlet velocity distribution given by Imam.[37] In the second case a higher flow rate (109·2 $cm^3\ s^{-1}\ cm^{-1}$) is used. The reattachment length is also calculated for various flow rates using the inlet profile. The reattachment length is in good agreement with the experimental data (Figure 14). Although the flow is highly turbulent, the reattachment length increases as the flow rate increases owing to the increase in the tank water depth with flow and the consequent increase in the baffle submergence.

An FTC represents the time response at the exit of a tank to a tracer pulse at the inlet. This curve is used for evaluating the hydraulic efficiency of settling tanks. As shown in Figure 15, the time axis has been normalized by the theoretical detention time $T_d = L^*H^*/q$ and the concentration axis by $C_0 = C_i \Delta t_i q/L^*H^*$, the concentration that would exist in the tank if all the tracer mass were completely mixed throughout the tank. The FTC calculations were carried out with STOUS (10 × 20, 10 × 40 and 20 × 40 grids) and UTOPIA (10 × 68 grid) for spatial discretization of the convection terms. Both UTOPIA and STOUS yielded the same solution. The FTC was found to be insensitive to

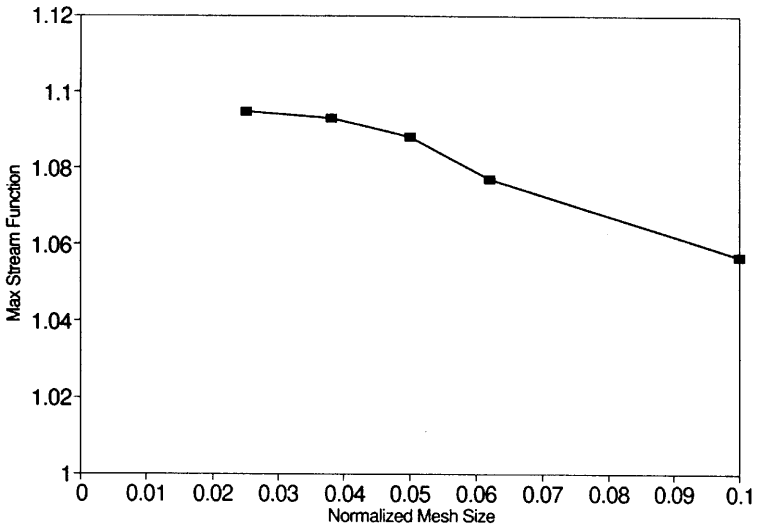

Figure 11. Effect of mesh size on maximum streamfunction Ψ_c at centre of recirulating zone

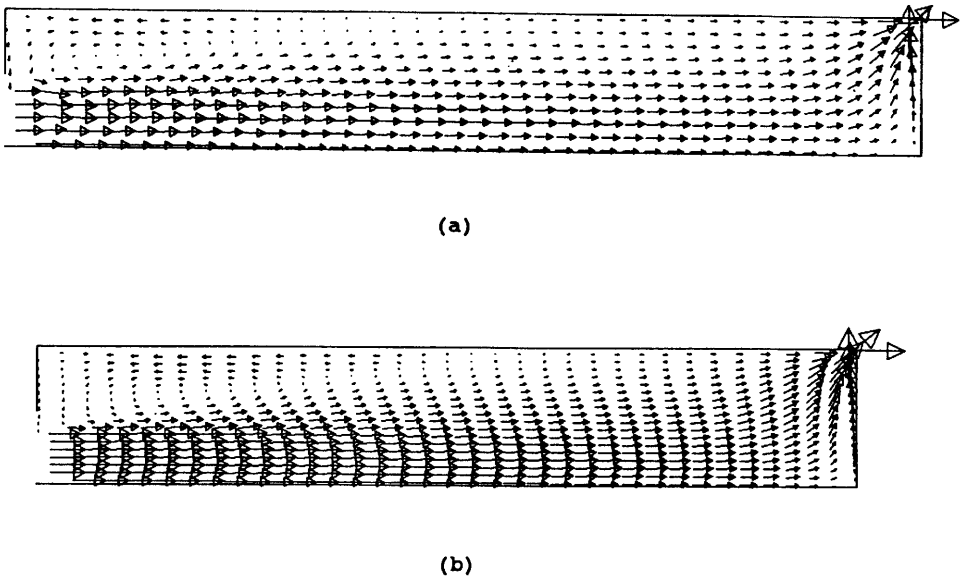

Figure 12. Predicted velocity field of Windsor clarifier:[37] (a) $Q = 37{\cdot}7$ cm^3 s^{-1} cm^{-1}, $L = 112$ cm, $H = 16{\cdot}5$ cm, $h_i = 8{\cdot}25$ cm, 10×40 grid, velocity scale 0·0–5·0; (b) $Q = 109{\cdot}4$ cm^3 s^{-1} cm^{-1}, $L = 73$ cm, $H = 11{\cdot}95$ cm, $h_i = 5.0$ cm, 17×34 grid, velocity scale 0·0–5·0

the time step variation as long as the Courant number was less than 0·3–0·5. Another mass transport model based on the HYBRID technique was developed. The hydrodynamic velocity and eddy viscosity fields predicted by STOUS were used for the HYBRID model. Figure 15 compares the predictions obtained by STOUS and HYBRID with experimental data of Imam.[37] STOUS overpredicts the FTC peak by 20% which could be due to the low mixing generated by the k–ϵ model. In the past, researchers have found that the k–ϵ overestimates the mixing in curved flows; however, some of this overestimation may have been due to numerical diffusion. Three-dimensional effects such as side boundary layers could result in higher mixing in the experiment. Comparison of HYBRID and STOUS suggests that the HYBRID results are subject to severe numerical diffusion.

The STOUS solution generated using a 10×20 grid agrees with the QUICK solution generated using a 25×25 grid.[29] Therefore STOUS could be considered as a coarse grid method, which implies that larger Δt-values can be used. It should also be noted that the use of implicit schemes (e.g. QUICK with ADI) may have less restrictive time step conditions, but is more expensive per time step because of iteration requirements.

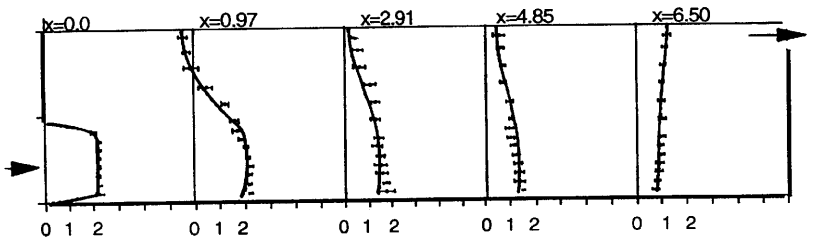

Figure 13. Comparision of predicted velocity field by STOUS and experimental data of Imam;[37] $Q = 45{\cdot}2$ cm^3 s^{-1} cm^{-1}, $L = 73$ cm, $H = 10{\cdot}3$ cm, $h_i = 4{\cdot}8$ cm, 17×34 grid

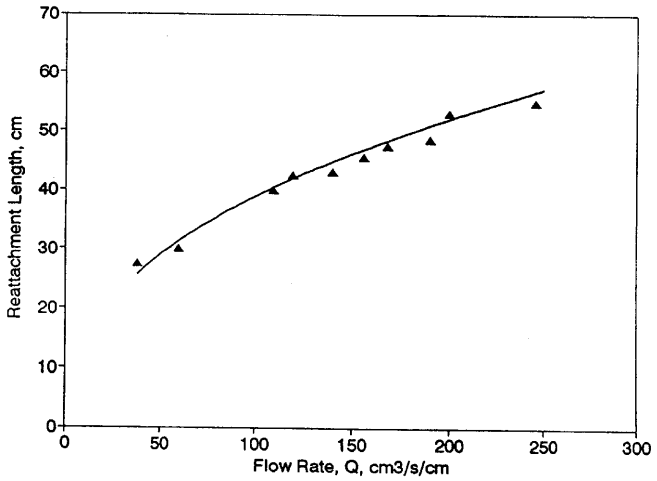

Figure 14. Variation in reattachemtn length with flow rate; $L = 73$ cm, $h_i = 4{\cdot}8$ cm: ▲, computed; ————, Imam's data[37]

4. CONCLUSIONS

The new numerical technique STOUS overcomes the instability and artificial diffusion problems of other numerical techniques while providing a wider stability range than UTOPIA; in addition, STOUS has been formulated for a grid aspect ratio 51, which is advantageous for flow in shallow tanks. For unsteady flows it gives much better accuracy than first-order upwinding for the same CPU cost. The algorithm has been verified with a benchmark test of 2D laminar flow past a backward facing step. STOUS has also been used to simulate the turbulent flow in settling tanks. The velocity predictions and reattachment lengths are in good agreement with the experimental data, which indicates that STOUS is capable of simulating steady recirculating turbulent flows.

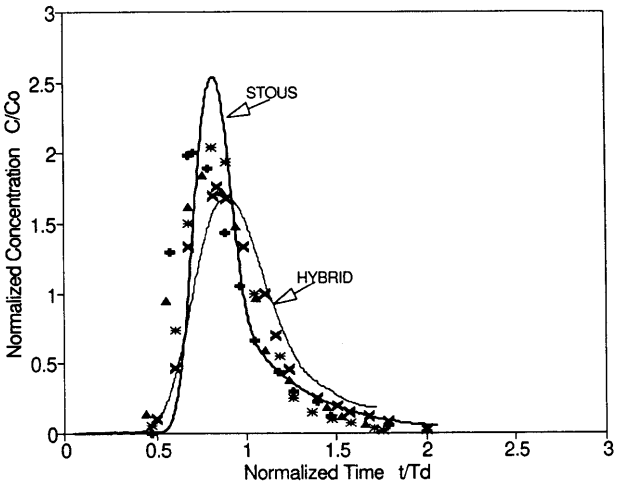

Figure 15. Comparision of predicted FTC using STOUS ($\sigma_c = 0{\cdot}7$) with dataq of Imam[37] (×, exp. A5; ▲ exp. A6; , exp. A8; +, exp. A9) and HYBRID scheme ($\sigma_c = 0{\cdot}7$)

STOUS has also been used to simulate the unsteady dye transport in settling tanks. STOUS adequately predicts the arrival and peak concentration time of the dye at the effluent weir but overpredicts the experimental FTC peak by 20%. A comparison of the HYBRID results with experimental data and the results of STOUS indicates that HYBRID suffers from high numerical diffusion, thus justifying the use of low-numerical-diffusion techniques such as STOUS or UTOPIA for problems such as dye transport.

ACKNOWLEDGEMENTS

This research was supported by a grant from the National Science and Engineering Research Council of Canada and a computer equipment grant from Rockwell International (Canada) Limited. H.G. was partially funded by an Ontario Graduate Scholarship.

APPENDIX I: STOUS FORMULATION

The west face formula is derived to show the approach. By choosing the interpolation points as shown in Figure 2(a), a triangle is formed assuming that Δx and Δy are constants but not necessarily equal. Introducing a local system of co-ordinates x and y (Figure 16), the six interpolation functions can be defined

$$
\begin{aligned}
N_{\mathrm{P}} &= 0{\cdot}5x(x-\Delta x)/(\Delta x)^2,\\
N_{\mathrm{W}} &= -1\cdot x(y\cdot\Delta x+\Delta y\cdot x-2\Delta y\cdot\Delta x)/\Delta y(\Delta x)^2,\\
N_{\mathrm{WW}} &= 0{\cdot}5(y\cdot\Delta x+\Delta y\cdot x-2\Delta y\cdot\Delta x)(y\cdot\Delta x+\Delta y\cdot x-\Delta y\cdot\Delta x)/(x)^2(\Delta y)^2,\\
N_{\mathrm{SW}} &= x\cdot y/\Delta y\cdot\Delta x,\\
N_{\mathrm{SWW}} &= -1\cdot y(y\cdot\Delta x+\Delta y\cdot x-2\Delta y\cdot\Delta x)/\Delta x(\Delta y)^2,\\
N_{\mathrm{SSWW}} &= 0{\cdot}5y(y-\Delta y)/(\Delta y)^2.
\end{aligned}
$$

To evaluate these interpolation functions at point O, the co-ordinates x and y of point O should be calculated. These co-ordinates are given as

$$(X_{\mathrm{O}}, Y_{\mathrm{O}}) = (1{\cdot}5\Delta x - C_x\Delta x/2, -C_y/2).$$

Substituting in (8) and arranging, the final formula (11) is obtained. For a complete west face computational stencil the new terms CURVTS and TWISTS for all flow cases are defined (Figure 17) as

$$
CURVTS = \begin{cases}
\phi_{\mathrm{SSWW}} - 2\phi_{\mathrm{SWW}} + \phi_{\mathrm{WW}} & \text{for} \quad C_x > 0 \text{ and } C_y > 0,\\
\phi_{\mathrm{SSE}} - 2\phi_{\mathrm{SE}} + \phi_{\mathrm{E}} & \text{for} \quad C_x < 0 \text{ and } C_y > 0,\\
\phi_{\mathrm{NNWW}} - 2\phi_{\mathrm{NNW}} + \phi_{\mathrm{WW}} & \text{for} \quad C_x > 0 \text{ and } C_y < 0,\\
\phi_{\mathrm{NNE}} - 2\phi_{\mathrm{NE}} + \phi_{\mathrm{E}} & \text{for} \quad C_x < 0 \text{ and } C_y* < 0,
\end{cases}
$$

$$
TWISTS = \begin{cases}
\phi_{\mathrm{SWW}} - \phi_{\mathrm{WW}} - \phi_{\mathrm{SW}} + \phi_{\mathrm{W}} & \text{for } C_x > 0 \text{ and } C_y > 0,\\
\phi_{\mathrm{SE}} - \phi_{\mathrm{E}} - \phi_{\mathrm{S}} + \phi_{\mathrm{P}} & \text{for } C_x < 0 \text{ and } C_y > 0,\\
\phi_{\mathrm{NWW}} - \phi_{\mathrm{WW}} - \phi_{\mathrm{NW}} + \phi_{\mathrm{W}} & \text{for } C_x > 0 \text{ and } C_y < 0,\\
\phi_{\mathrm{NE}} - \phi_{\mathrm{E}} - \phi_{\mathrm{N}} + \phi_{\mathrm{P}} & \text{for } C_x < 0 \text{ and } C_y < 0,
\end{cases}
$$

The south face formula and corresponding terms are defined in the same manner.

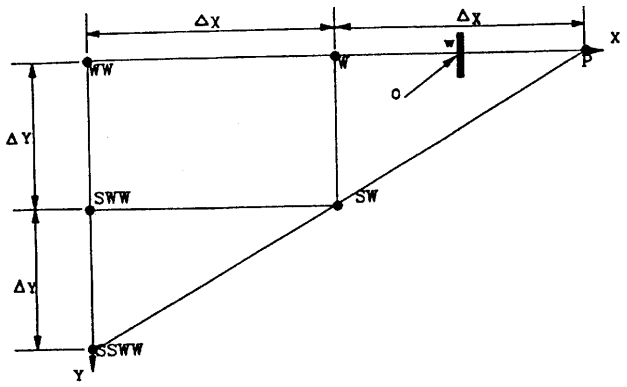

Figure 16. West face interpolation triangle for $u, v > 0{\cdot}0$

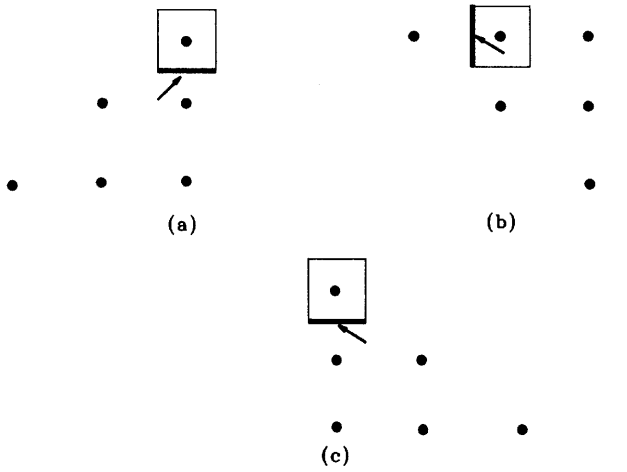

Figure 17. Computational stencils: (a) south face for $u, v > 0{\cdot}0$; (b) west face for $u < 0{\cdot}0, v > 0{\cdot}0$; (c) south face for $u0{\cdot}0, v > 0{\cdot}0$

APPENDIX II: AMPLIFICATION FACTOR

STOUS

Referring to Figure 2, the Fourier component of the solution at point P is given as

$$\phi_{\mathrm{P}}^{n} = V^{n} \mathrm{e}^{Ii\theta_x} \mathrm{e}^{Ij\theta_y}. \tag{49}$$

The components at points E, W, N, S, WW, SW, NW and SSWW can likewise be determined. Substituting the Fourier component into the convection–diffusion equation (3) results in a complicated expression; therefore each term of (3) will be presented separately. The convection

term in the x-direction can be re-written as

$$
\begin{aligned}
-C_x(\phi_e-\phi_w) = {} & -C_x\frac{\phi_E-\phi_W}{2}+\frac{C_x^2}{2}(\phi_E-2\phi_P+\phi_W)\\
& +\left(\frac{C_x}{8}-\frac{C_x^3}{8}-\frac{C_x\alpha}{2}\right)(\phi_E-3\phi_P+3\phi_W-\phi_{WW})\\
& +\frac{C_xC_y}{2}(\phi_P-\phi_S-\phi_W+\phi_{SW})\\
& -\left(\frac{C_xC_y^2}{8}-\frac{C_xC_y}{4}+\frac{C_x\alpha}{2}\right)(\phi_{SSW}-2\phi_{SW}+\phi_W-\phi_{SSWW}+2\phi_{SWW}-\phi_{WW})\\
& -\left(\frac{C_x^2C_y}{4}-\frac{C_xC_y}{4}\right)[2(\phi_{SW}-\phi_W)-(\phi_S-\phi_P)-(\phi_{SWW}-\phi_{WW})], \qquad (50)
\end{aligned}
$$

in which

$$\frac{\phi_E-\phi_W}{2}=V^n e^{Ii\theta_x}e^{Ii\theta_y}(I\sin\theta_x), \qquad (51)$$

$$\phi_E-2\phi_P+\phi_W=V^n e^{Ii\theta_x}e^{Ij\theta_y}[-2(1-\cos\theta_x)], \qquad (52)$$

$$\phi_E-3\phi_P+3\phi_W-\phi_{WW}=V^n e^{Ii\theta_x}e^{Ij\theta_y}(4\cos\theta_x-2I\sin\theta_x-\cos 2\theta_x+I\sin 2\theta_x-3), \qquad (53)$$

$$
\begin{aligned}
\phi_P-\phi_S-\phi_W+\phi_{SW} = {} & V^n e^{Ii\theta_x}e^{Ij\theta_y}[1-\cos\theta_x-\sin\theta_x\sin\theta_y+I\sin\theta_x(1-\cos\theta_y)\\
& +I\sin\theta_y(1-\cos\theta_x)-\cos\theta_y(1-\cos\theta_x)], \qquad (54)
\end{aligned}
$$

$$
\begin{aligned}
&\phi_{SSW}-2\phi_{SW}+\phi_W-\phi_{SSWW}+2\phi_{SWW}-\phi_{WW}\\
&\quad = V^n e^{Ii\theta_x}e^{Ij\theta_y}[(\cos 2\theta_y-I\sin 2\theta_y)(\cos\theta_x-I\sin\theta_x)-2(\cos\theta_y-I\sin\theta_y)(\cos\theta_x-I\sin\theta_x)\\
&\qquad +(\cos\theta_x-I\sin\theta_x)-(\cos 2\theta_y-I\sin 2\theta_y)(\cos 2\theta_x-I\sin 2\theta_x)\\
&\qquad +2(\cos\theta_y-I\sin\theta_y)(\cos 2\theta_x-I\sin 2\theta_x)-(\cos 2\theta_x-I\sin 2\theta_x)]. \qquad (55)
\end{aligned}
$$

The convection term in the y-direction can be similarly derived. The diffusion term in the x-direction can be rewritten as

$$
\begin{aligned}
\alpha\left[\left(\frac{\partial\phi}{\partial x}\right)_e-\left(\frac{\partial\phi}{\partial x}\right)_w\right]\Delta x = {} & \alpha\left(2\cos\theta_x-2-\frac{C_x}{2}[-2(1-\cos\theta_x)^2+2I\sin\theta_x(1-\cos\theta_x)]\right.\\
& \left.-\frac{C_y}{2}[2(\cos\theta_x-1)(1-\cos\theta_y)+2I\sin\theta_y(\sin\theta_y(\sin\theta_x-\cos\theta_y)]\right) \qquad (56)
\end{aligned}
$$

and similarly the diffusion coefficient in the y-direction can be determined. The amplification factor equation for STOUS is obtained by combining these terms in one expression.

UTOPIA

The convection term in the x direction is

$$\begin{aligned}-C_x(\phi_e-\phi_w) = &-C_x\frac{\phi_E-\phi_W}{2}+\frac{C_x^2}{2}(\phi_E-2\phi_P+\phi_W)\\ &+\left(\frac{C_x}{6}-\frac{C_x^3}{6}-\frac{C_x\alpha}{2}\right)(\phi_E-3\phi_P+3\phi_W-\phi_{WW})\\ &+\frac{C_xC_y}{2}(\phi_P-\phi_S-\phi_W+\phi_{SW})\\ &-\left(\frac{C_xC_y^2}{6}-\frac{C_xC_y}{4}+\frac{C_x\alpha}{2}\right)(\phi_N-2\phi_P+\phi_S-\phi_{NW}+2\phi_W-\phi_W)\\ &-\left(\frac{C_x^2C_y}{3}-\frac{C_xC_y}{4}\right)[(\phi_E-\phi_{ES})+(\phi_W-\phi_{SW})-2(\phi_P-\phi_S)],\end{aligned} \tag{57}$$

to which

$$\begin{aligned}\phi_N-2\phi_P+\phi_S-\phi_{NW}+\phi_W-\phi_{SW} = V^n e^{Ii\theta_x}e^{Ij\theta_y}[&-2(1-\cos\theta_y)(1-\cos\theta_x)\\ &+2I(\cos\theta_y-\sin\theta_x)],\end{aligned} \tag{58}$$

$$\begin{aligned}\phi_E-\phi_{ES}+\phi_W-\phi_{SW}-2\phi_P+2\phi_S = V^n e^{Ik\theta_x}e^{Ij\theta_y}[&2\cos\theta_x(1-\sin\theta_y)-2(1-\cos\theta_y)\\ &-2I\sin\theta_y(1-\cos\theta_x)].\end{aligned} \tag{59}$$

The diffusion terms for UTOPIA are the same as for STOUS.

REFERENCES

1. A. R. Mitchell, 'Recent developments in the finite element method', in J. Noye and C.A. Fletcher (eds), *Computational Techniques and Applications: CTAC-83*, P. 21. Elsevier/North-Holland, Amsterdam, 1984, p. 21.
2. R. Courant, E. Isaacson and M. Rees, 'On the solution of nonlinear hyperbolic differential equations by finite difference', *Commun. Pure Appl. Math.*, **5**, 243 (1952).
3. B. P. Leonard and H. S. Niknafs, 'Sharp monotonic resolution of discontinuities without clipping of narrow extrema', *Comput and Fluids*, **19**, 141–154 (1991).
4. J. E. Fromm, 'A method for reducing dispersion in convective difference schemes', *J. Comput. Phys.*, **3**, 176–189 (1968).
5. P. D. Lax and B. Wendroff, 'Systems of conservation laws', *Commun. Pure Appl. Math.*, **13**, 217–237 (1960).
6. B. P. Leonard, 'A stable and accurate convective modelling procedure based on quadratic upstream interpolation', *Comput. Methods Appl. Mech. Eng.*, **19**, 59–98 (1979).
7. M. A. Leschziner, 'Modeling turbulent recirculating flows by finite-volume methods—current status and future directions', *Int. J. Heat Fluid Flow*, **10**, 186–202 (1989).
8. J. Glass and W. Rodi, 'A higher order numerical scheme for scalar transport', *Comput. Methods. Appl. Mech. Eng.*, **33**, 337–358 (1982).
9. B. P. Leonard, 'Adjusted quadratic upstream algorithms for transient incompressible convection', *Proc. 4th AIAA Computational Fluid Dynamics Conf.* Williamsburg, VA, 1979, AIAA, New York, 1979, pp. 292–299.
10. A. G. F. Nasser and M. A. Leschziner, 'Computation of transient recirculating flow using spline approximation and time space characteristics', *Proc. 4th Int. Conf. on Numerical Methods in Laminar and Turbulent Flows*, Swansea, 1985, pp. 480–491.
11. B. P. Leonard, 'Third order upwinding as a rational basis for computational fluid dynamics, in J. Noye and C. A. J. Fletcher (eds), *Computational Techniques and Application: CTAC-83*, Elsevier/North-Holland, Amsterdam, 1984, p. 106.
12. M. A. Leschziner and W. Rodi, 'Calculation of annular and twin parallel jets using various discretization schemes and turbulence model variations', *J. Fluids Eng., Trans. ASME*, **103**, 352–360 (1981).
13. B. P. Leonard, 'The ULTIMATE conservative difference scheme applied to unsteady one-dimensional advection', *Comput. Methods Appl. Mech. Eng.*, **88**, 17–74 (1991).
14. C. E. Leith, 'Numerical simulation of the earth's atmosphere', *Methods Compit. Phys.*, **4**, 1–28 (1965).
15. B. P. Leonard and H. S. Niknafs, 'Cost effective accurate coarse-grid method for highly convective multidimensional unsteady flow', *Proc. CFD Symp. on Aeropropulsion*, Cleveland, OH, 1990.

16. P. L. Roe, 'Characteristic-based schemes for the Euler equations', *Ann. Rev. Fluid Mech.*, ***18 (1986).***
17. C. A. J. Fletcher, *Computational Techniques for Fluid Dynamics*, Vols I and II, Springer, Berlin, 1988.
18. B. P. Leonard, 'Note on the von Neumann stability of the explicit FTCS convective diffusion equation', *Appl. Math. Model.*, **4**, 401–402 (1980).
19. L. Ekebjaerg and P. Justesen, 'An explicit scheme for advection–diffusion modelling in two dimensions', *Comput. Methods Appl. Mech. Eng.*, **88**, 287–297 (1991).
20. P. J. Rasch, 'Conservative shape-preserving two dimensional transport on a spherical reduced grid', *Mon. Weather Rev.*, **122**, 1337–1350, (1994).
21. B. P. Leonard, 'The flux integral method for multidimensional convection and diffusion', *Appl. Math. Model.*, **19**, 333–342, (1995).
22. D. R. Schamber and B. E. Larock, 'Numerical analysis of flow in sedimentation tanks', *J. Hydraul. Div. ASCE*, **107** 575–591 (1981).
23. E. Imam and J. A. McCorquodale, 'Simulation of flow in rectangular clarifiers', *J. Environ. Eng. ASCE*, **109**, 713–730 (1983).
24. S. M. Abdel Gawad and J. A. McCorquodale, 'Strip integral method applied to settling tanks', *J. Hydraul. Eng. ASCE*, **110**, 1–17 (1984).
25. I. Celik, W. Rodi and A. Stamou, 'Predictions of hydrodynamic characteristics of rectangular settling tanks', *Proc. Int. Symp. on Refined Flow Modeling and Turbulence Measurements*, Iowa City, IA, 1985, 641–651.
26. M. Casonato and F. Gallerano, 'A finite difference self-adaptive mesh solution of flow in a sedimentation tank', *Int. j. num. meths. fluids*, **10**, 697–711 (1990).
27. B. A. Devantier and B. E. Larock, 'Modelling sediment induced density current in sedimentation tanks', *J. Hydraul. Eng. ASCE*, **113**, 80–94 (1987).
28. S. Zhou and J. A. McCorquodale, 'Modeling of rectangular settling tanks', *J. Hydraul. Eng. ASCE*, **188**, 1391–1405 (1992).
29. E. W. Adams and W. Rodi, 'Modeling flow and mixing in sedimentation tanks', *J. Hydraul. Eng., ASCE*, **116**, 895–913 (1990).
30. L. Szalai, P. Krebs, and W. Rodi, 'Simulation of flow in circular clarifiers with and without swirl', *J. Hydraul. Eng. ASCE*, **120**, 4–21 (1994).
31. B. P. Leonard, 'Elliptic systems: finite difference method IV, in W. J. Minkowicz *et al.* (eds), *Handbook of Numerical Heat Transfer*, Wiley, New York, 1988, pp.347–378.
32. B. F. Armaly, F. Durst, J. C. F. Pereira and B. Schonung, 'Experimental and theoretical investigation of backward-facing step flow', *J. Fluid Mech.*, **127**, 473–496 (19xx).
33. W. Rodi, *Turbulence Models and Their Application in Hydraulics. A State-of-the Art Review*, International Association for Hydraulic Research, Delft, 19xx.
34. ASCE Task Committee on Turbulence Modelling Models in Hydraulic Computation, 'Turbulence modelling of surface water flow and transport: Part II', *J. Hydraul. Eng. ASCE*, **114**, 992–1014 (1988).
35. A. D. Gosman and W. M. Pun, 'Calculation of recirculating flows', *HTS//2*, Imperial College, London, 1974.
36. B. P. Leonard and S. Mokhtari, 'Beyond first-order upwinding: the ULTRA-SHARP alternative for non-oscillatory steady state simulation of convection', *Int. j. numer. methods eng.*, **30**, 729–766 (1990).
37. E. Imam, 'Numerical modeling of rectangular clarifiers', *Ph.D. Thesis*, University of Windsor, 1981.

